Journal of Sound and Vibration (2002) **252**(4), 591–615
doi:10.1006/jsvi.2001.4037, available online at http://www.idealibrary.com on IDEAL®

EXPERIMENTAL VERIFICATION OF STRUCTURAL-ACOUSTIC MODELLING AND DESIGN OPTIMIZATION

S. Marburg, H.-J. Beer, J. Gier and H.-J. Hardtke

Institut für Festkörpermechanik, Technische Universität, 01062 *Dresden, Germany*.
E-mail: *marburg@mfm.mw.tu-dresden.de*

R. Rennert

Institut für Materialforschung und Anwendungstechnik GmbH, 01101 *Dresden, Germany*

AND

F. Perret†

*Ecole Supérieure de Mécanique de Marseille, IMT – Technopole de Chateau–Gombert, F–*13451 *Marseille Cedex* 20, *France*

(*Received* 30 *May* 2000, *and in final form* 23 *August* 2001)

A number of papers have been published on the simulation of structural-acoustic design optimization. However, extensive work is required to verify these results in practical applications. Herein, a steel box of $1{\cdot}0 \times 1{\cdot}1 \times 1{\cdot}5$ m with an external beam structure welded on three surface plates was investigated. This investigation included experimental modal analysis and experimental measurements of certain noise transfer functions (sound pressure at points inside the box due to force excitation at beam structure). Using these experimental data, the finite element model of the structure was tuned to provide similar results. With a first structural mode at less than 20 Hz, the reliable frequency range was identified up to about 60 Hz. Obviously, the finite element model could not be further improved only by mesh refinement. The tuning process will be explained in detail since there was a number of changes that helped to improve the structure. Other changes did not improve the structure. Although this model of the box could be expected as a rather simple structure, it can be considered to be a complex structure for simulation purposes. A defined modification of the physical model verified the simulation model. In a final step, the optimal location of stiffening beam structures was predicted by simulation. Their effect on the noise transfer function was experimentally verified. This paper critically discusses modelling techniques that are applied for structural-acoustic simulation of sedan bodies.

1. INTRODUCTION

Several papers that deal with structural-acoustic optimization indicate significant improvements of the acoustic properties inside or outside the structure. Noise reductions of 10–50 dB have been reported. Most of them will be discussed in what follows.

Hambric [1, 2] reported the reduction of the emitted sound power of a ribbed cylindrical shell with hemispherical ends over a large frequency range by about 10 dB using location of ribs, shell thickness and loss factors as parameters. Similarly, Lamancusa [3, 4] indicated 8–15 dB reduction in a frequency range (100–1000 Hz) only by optimizing the local

† Work carried out during this author's trainee period at the Institut für Festkörpermechanik.

0022-460X/02/$35.00

distribution of plate thickness at a constant mass. In an earlier paper, Lamancusa [5] discussed minimization of noise transmission through an intake system of internal combustion engines. While optimally designing diameters and lengths of ducts, he managed to reduce the average noise transmission by up to 20 dB over a frequency range of 50–250 Hz. Experimental verification was provided.

In his dissertation, Hibinger [6] discussed optimization problems of two plates perpendicularly oriented to each other. First, he verified the calculation model with an existing physical model. Then he optimized structure-borne noise in these plates by a locally distributed plate thickness and ribs. Experimental verification was also provided for the optimized structure. He presented similar investigations for a box structure. It was mentioned that more than 10 dB average reduction over a large frequency range was achieved in real structures. Experimental measurements of optimized structures were not reported. However, once a reliable simulation model is available, this model should be reliable for the modified structure as well.

Pal and Hagiwara *et al.* [7–9] presented an example where they observed an improvement of about 50 dB in a box only by optimizing the plate thickness of flat panels. Tinnsten, *et al.* [10] reported similar reduction of noise inside a box structure. They applied locally distributed plate thicknesses and the fibre orientation as optimization parameters. In most of the papers that optimize plate thickness distributions, at least one constraint concerning an upper limit of the mass was necessary and, therefore, included. Experimental investigations have been reported by Tinnsten [11]. In that paper, optimization of radial thickness distribution of a circular plate was simulated and experimentally verified.

In their papers, Cunefare and Engelstad *et al.* [12–14] describe the minimization of sound transmission through a cylindrical shell that is clamped at both ends. Application of 20 optimization variables [12] that represented 20 circumferential bands of constant thickness allowed them to reduce the transmission level by about 20 dB while keeping the mass constant. With respect to these results, they emphasized the particular value of structural-acoustic optimization in passive noise control. In references [13, 14], they presented the results of optimal geometry and cross-sectional shapes of frames and stringers. A reduction of 8·6 dB was gained mainly by optimizing the geometry of the stiffening structures over the cylinder. Cross-sections of the stiffeners were of minor importance in the optimization process.

Belegundu and Koopmann *et al.* [15–19] have reduced the radiated sound power of plates and shells. In one of these papers [15], a plate of optimized stepped thickness distribution confirmed that even a weaker structure can radiate less sound than a stiffer structure. In that example, the first eigenfrequency of an engine cover plate was decreased while the radiated noise level was reduced by about 12 dB. Similar investigations [17] were reported for piecewise constant material data like Young's modulus or density. Reductions between 2 and 23 dB were achieved. Optimally sized discrete masses [18] lead to an improvement of 30 dB in the simulation and, still, 22 dB in the experiment. Although this can be considered as a good prediction, the authors discussed the differences between theoretical and experimental results. In the special cases of a clamped plate and a semicylindrical shell [16], reductions of 33 dB for the clamped plate and 9·6 dB for the shell were gained by adding lumped masses. Both the position of the masses and their size were considered in their investigation. In another paper by these authors [19], results of simulated optimization for a half–cylindrical shell were compared with the experimental data. Finally, it was stated that a next task should involve more realistic and, therefore, more complex structures.

There are few papers dealing with shape modification of the shell curvature. In their work on optimization of the directivity pattern of a loudspeaker, Christensen and Olhoff [20]

manage to change the original directivity pattern at different frequencies simultaneously by 10–20 dB. In that paper, eight keypoint positions and locally distributed shell thicknesses occurred as design parameters. The papers by Marburg and Hardtke *et al.* [21–23] indicate that significant reduction of noise emission is possible only by changing the curvature of a shell structure. If this modification remains small with respect to a characteristic dimension of the shell, then the mass remains nearly constant. Hence, a mass constraint is negligible.

Considering very complex structures, in general, and vehicle bodies, in particular, the most challenging problem arises in creating a reliable calculation model. Obviously, this model should be a compromise. It should be simple enough to be handled easily and to avoid unnecessary expensive computation especially in the optimization process and it should be detailed enough to represent all or at least most of the desired effects being under consideration. Modelling of the body structure of a car usually is so complex that existing local effects of vibration cannot reliably be validated in the calculation model. Moreover, methods that proposed changes of the geometry of vehicle panels [21, 22] cannot be verified with these structures. The possibility of substituting the panel by another panel with new geometry would include a destruction of the complex structure and even an identical panel would provide a new vibroacoustic behaviour. An alternative would be to produce two body structures, one with the original and one with the optimized panel. However, it is well-known that in the case of complex structures we will hardly find two identical compositions. Thus, the improvement of complex structures can only show an average effect for a large set of examples.

For that reason, a simpler structure is chosen to verify improvements of structural optimization experimentally. This construction consists of two beam frames and six more or less flat panels. Together they form a box with an external beam construction. In general, the components are welded together to have a vehicle body like assembly. To avoid destruction of the box, feasible design modifications only include addition of stiffening beam structures.

In this paper, the authors will discuss the process of finding a reliable calculation model in a reasonable period of time. The simulation model is tuned with respect to modes found in the experimental modal analysis. Further, experimentally measured structural and noise transfer functions give an impression of the reliability of the simulation model. This frequency range of reliability is confirmed by an added mass block that was used to imply a defined modification. Finally, the model will be modified by four added beams of optimized length and position. All model modifications will be experimentally verified.

Experiments and analysis are limited to a frequency range of 0–100 Hz. The upper limit correlates to initial expectations that could not be accomplished.

2. MODEL DESCRIPTION

2.1. PHYSICAL MODEL

The physical model was designed and constructed for experimental purposes. It was assembled in a similar way as a sedan body is made. This includes welding spots and welding joints. This was confirmed by the automotive company that constructed the model. However, exactness of the assembly was somewhat rougher than those of real cars.

The box-like model consists of an internal beam-frame, an external frame structure and six surface panels. It is made of steel. The internal frame and the surface metal sheets are spot-welded together. The independently completed external frame is fixed at the surface panels at certain welding joints. Owing to welding points, welding joints and additional

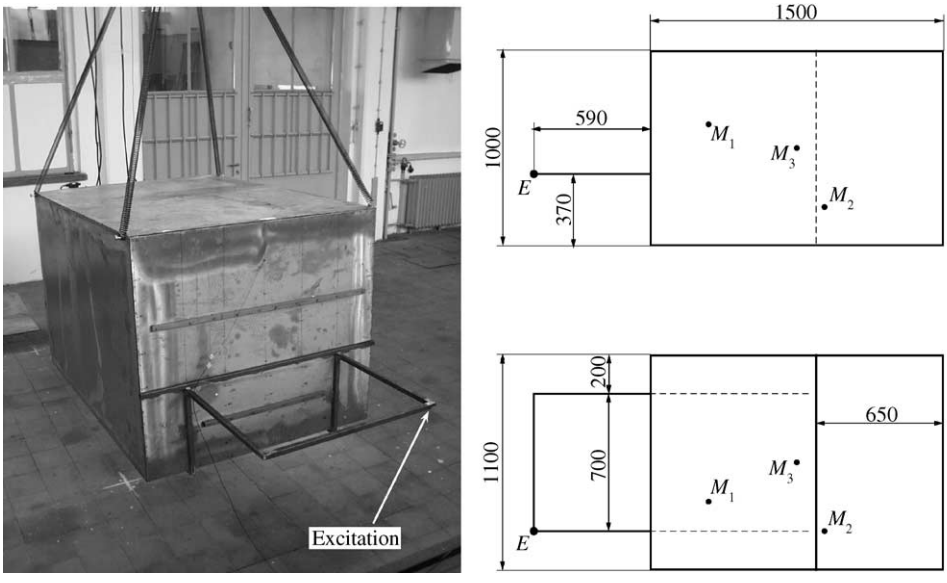

Figure 1. Left: photograph of the box, two beams on the front panel show positions of optimized stiffeners. Right: drawing of the structural model (measures in mm), view from the left (upper subfigure) and from above (lower subfigure), positions of three microphones indicated by M_1, M_2 and M_3, location of excitation marked by letter E.

prestrain effects, it can be easily observed that the surface panels are not as plane as it could be expected for a simple structure. Gaps between the external frame and the distorted plates range between 0 and 5 mm. These distortions can be observed for all panels with the exception of the rear panel.

A photograph of the structure is shown in Figure 1. In the right subfigures, two simplified drawings give a vivid description of the dimensions of the model. The end of the external frame will be called the front end. Not only does the internal frame support the edges of the box but there is an additional frame belt as can be seen in the drawings in Figure 1. The upper and the lower adjacent surface panels have a gap along this frame belt. Both parts, are detached from each other but spot–welded at the frame belt. The side panels are continuous from the front to the rear. The rear panel can be dismounted since it is screwed to the base–frame. The external beam structure stiffens the lower part of the front panel and the front part of the floor panel.

The panels are of different thicknesses between 1·2 and 3 mm while the beam structure has a 20 mm square cross-section of 2 mm thickness.

The support conditions can be considered to be free–free. Four elastic suspensions on soft tensions springs are used for that (cf. photograph in Figure 1). They are fixed at the upper corners. These points are of particular stiffness so that the support conditions should hardly influence the elastic vibration modes. Six rigid-body modes are expected. These modes can actually be identified. The maximum eigenfrequency of a rigid body mode is found at about 4 Hz and the lowest elastic mode is observed above 19 Hz.

The force excitation is applied at the left corner of the external beam frame in front of the box. This ensures that the force excitation does not directly act on a noise-emitting panel. This will be similar to engine excitation of cars. Moreover, the external beam frame transmits the structural vibrations to the front of the lower panel. The remaining four panels are excited by these two.

Three holes have been bored into the upper panel. These holes are required for sound pressure measurements inside the box. Their diameter is about 30 mm, just sufficient to conduct one hanging microphone through.

2.2. SIMULATION MODEL

For simulation purposes, a geometry-based model has been created for the structure. This model consists of 583 keypoints. Connection of these keypoints are realized using 1134 spline-interpolated lines while these lines form 572 interpolated areas. The panel surfaces are modelled with variable curvature to include the uneven characteristics of these areas. All panels and even the beam structures are included as areas although it could be assumed that modelling of beams as lines would be sufficient for our purposes. However, especially the spatially distributed cross-sections of the beams and, henceforth, the chance of spatially distributed and selective coupling between beams and surface panels appeared to be a particular sensitive issue in the process of model adjustment.

One of the advantages of a geometry-based model is the possibility of variable meshes. Checking different mesh sizes, we finally end up with a compromise of a maximum shell element size of 5 cm, i.e., there are many smaller elements. Altogether the finite element model of the structure consists of 6577 (linear) shell elements and about 6604 nodes. Figure 2 supplies a more vivid description of the geometry-based model and the finite element mesh.

The constraints between the three different parts of the structure are modelled as very short and light but stiff beams. The commercial finite element code ANSYS [24] that is used for structural analysis offers usage of constraint equations as well. However, in this case they provide a 10 times greater wavefront in the solution process. The simulation model contains

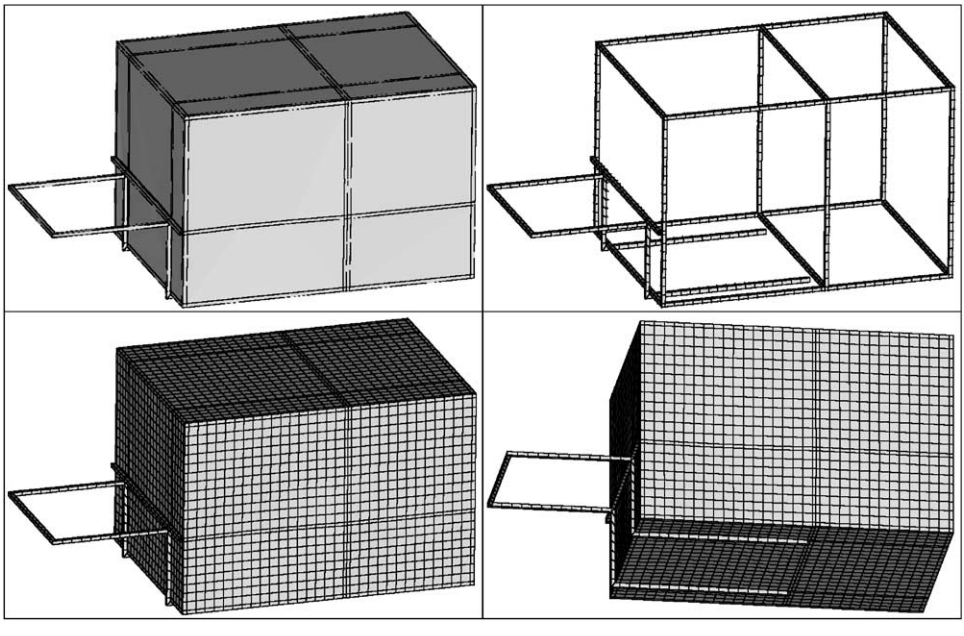

Figure 2. Visualization of structural model, area plot (upper left), beam frame elements (upper right) and complete model of element size $\leqslant 5$ cm (lower subfigures).

1235 of these short beam elements. This approach of modelling welds is utilized currently in low-frequency finite element analyses of vehicle body models, cf. Vlahopoulos *et al.* [25].

To briefly discuss a refined mesh of the structure that will be referred to in the modal analysis section, we mention that this model consists of 18 773 linear shell elements of size $\leqslant 2{\cdot}5$ cm while the number of nodes reaches 18 836. Compared with the coarser model, the wavefront in the solution process increases from 1830 to 2370.

The fluid model is much coarser than the model of the structure. It consists of 850 linear boundary elements and 852 nodes. That is equivalent to an element size of 10 cm. With the material data of air being 340 m/s as the speed of sound and $1{\cdot}3$ kg/m^3 as the fluid's density and an upper frequency limit of 100 Hz, we have 34 elements per wavelength. Even with the knowledge of a bad convergence of linear acoustic elements [26, 27], one can expect very small numerical errors for the fluid analysis. Generally, the boundary conditions for the fluid are assumed to be rigid. One test will be described where the fluid's boundary conditions include complex boundary admittances.

The (non-commercial) boundary element-based computer program Akusta is used for the acoustic calculations. Akusta allows the computation of acoustic influence coefficients that can be efficiently used for optimization purposes [22, 28].

It shall be mentioned that for this type of multi-field calculation, a one-way fluid structure interaction is assumed. This includes that we first compute the structural vibrations in vacuum and, then, take the harmonic particle velocity distribution as a boundary condition for an acoustic analysis.

3. EXPERIMENTAL AND SIMULATED MODAL ANALYSIS

It is well-known that especially simulation models initially show many differences in their vibration behaviour when compared with the real model. This dilemma increases for complex models. Moreover, it seems beyond a reasonable solution if large numbers of modes should be considered. Although initially a simple model was looked for, we obviously have to expect numerous eigenfrequencies in the frequency range up to about 100 Hz.

The comparatively stiff edges of the box can likely be assumed to be one of the major advantages of this model for low frequencies. Hence, it is possible to consider most of the surfaces separately. This is a reasonable simplification for the first one or two modes of each panel. However, hardly any useful success may be reported in some cases even for low frequencies.

For the experimental modal analysis, the left corner of the external beam frame in front of the box is excited by an impact hammer, types B&K 8202. Piezoelectric accelerometers of types B&K 4374 having a negligible mass of about 1 g. A B&K analyzer type 3550 was used.

The experimental modal analysis of the structure considers accelerations at 70 positions. Major focus is on the vibrations of the front panel and the external beam frame. They contain 23 positions where vibrations have been measured. The remaining 47 positions are evenly distributed over the other five panels. A more detailed modal analysis especially using a laser scanning vibrometer would have been useful for this investigation especially for the vibrations of the flat shell panels.

Several different measures are taken to match modes and frequencies of simulation and experimental modal analysis. Most successful changes include:

- optimization of panel curvature, especially front panel,
- prestrain effects at welding joints,
- carefully incorporated coincidence of welding spots/joints and beam constraints,
- adjustment of panel thicknesses.

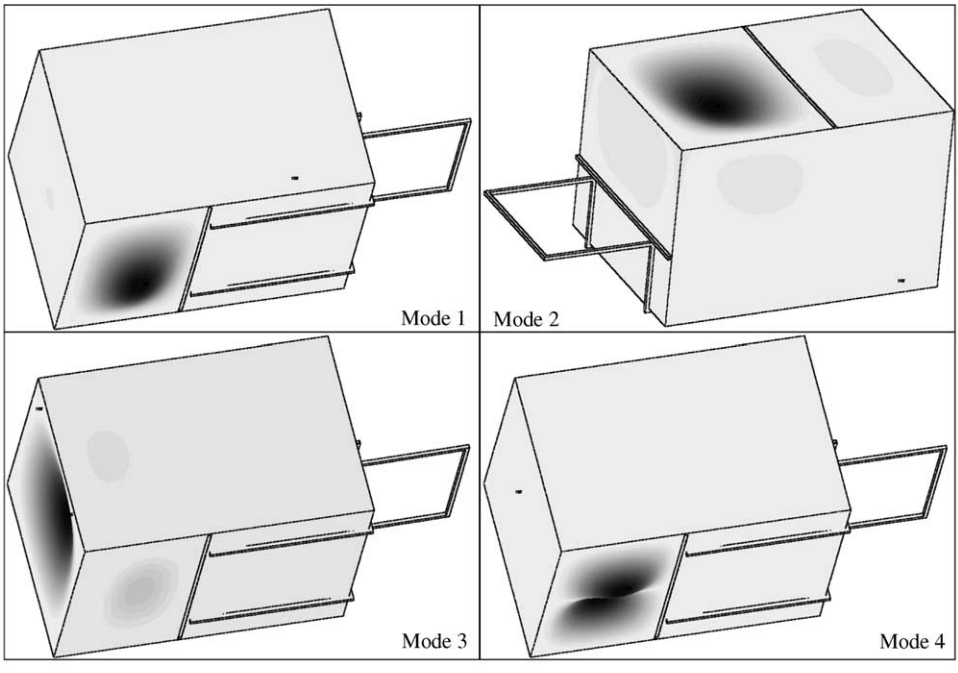

Figure 3. Modes 1–4 (19·3, 20·2, 23·7, 27·8 Hz) of the box model, frequencies of the experimental and simulated modal analyses in Table 1.

A number of additional trials have been realized, for example incorporation of self-weight. However, the above given items are best suited to adjust the calculation model.

Now we would discuss the results of the experimental and the simulated modal analysis. The experimental modal analysis provides about 20 modes. Obviously, the lowest six modes are subject to rigid-body modes. Most of the remaining 14 modes can be identified in the simulated modal analysis.

Twelve mode shapes are visualized in Figures 3–5. Eigenfrequencies in the order of occurrence in the simulation can be found in Table 1. An excellent agreement for most of the eigenfrequencies is observed. The worst deviation occurred for mode 4, the second mode of the rear floor panel. It is assumed that this is subject to welding joints between this panel and the internal base frame. Modes 2 and 3 are calculated very close to the experimentally determined frequencies. Though modes 6 and 7 look very similar and can even be found at neighbouring frequencies, they are both confirmed by the experimental data. Mode 8 cannot be verified in the experimental modal analysis. This may happen because the number of accelerometers in this domain chosen is too small. However, there are two modes below 40 Hz in the experiment that cannot be identified. So this problem can also be originated by an inconsistency of the experimental data. For more explanations on this subject, see reference [29]. Another reason may be that these modes have not been excited. This is unlikely because, in general, vibrations of all panel are observed when the external frame is excited. But this argument cannot be excluded. Another typical mode shape is mode 9. While for lower frequencies usually, only one panel accounts for a single vibration mode shape, higher modes are characterized by global eigenvector shapes. These global modes are much more difficult to adjust.

Good and important mode matching can be reported for the external frame structure and the front panel. Adjustment of beam modes 5 and 22 requires exact positioning of the

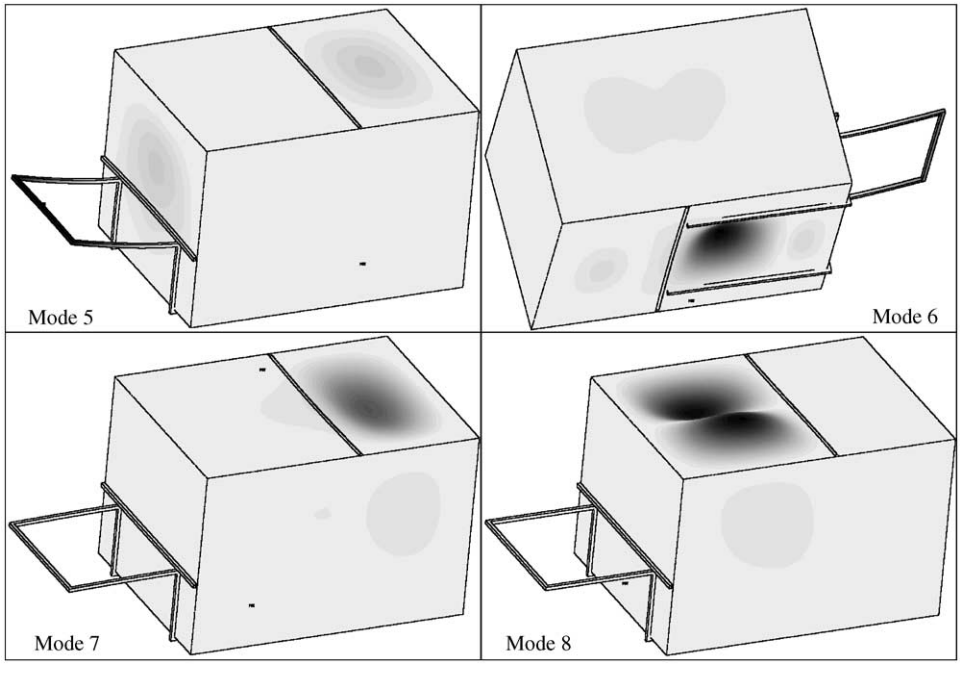

Figure 4. Modes 5–8 (28·1, 28·6, 29·8, 35·5 Hz) of the box model, frequencies of the experimental and simulated modal analyses in Table 1.

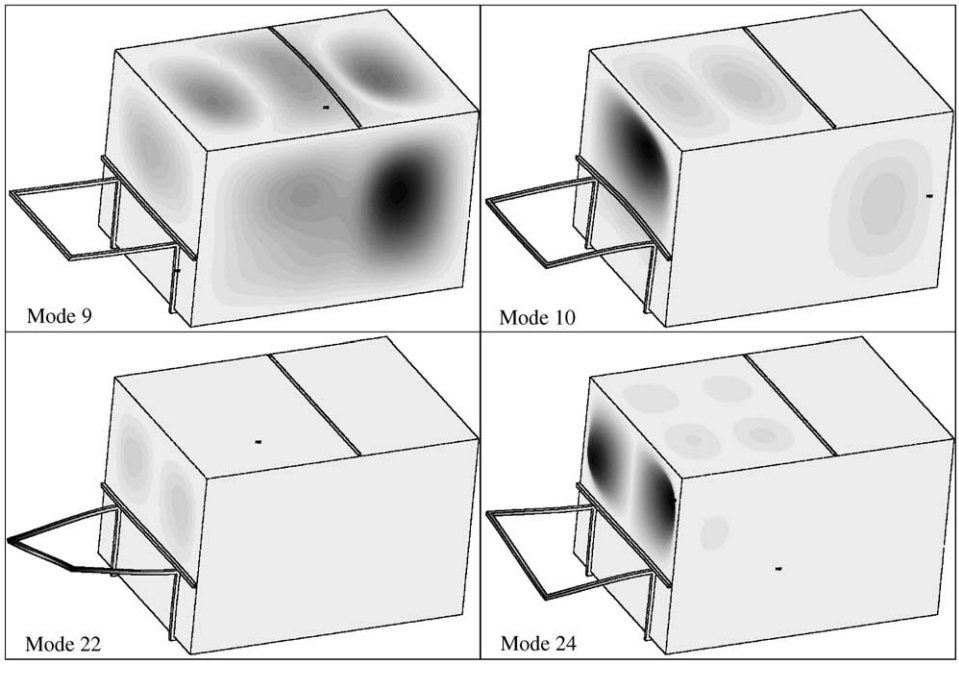

Figure 5. Modes 9 (36·9 Hz), 10 (38·2 Hz), 22 (54·2 Hz) and 24 (56·6 Hz) of the box model, frequencies of the experimental and simulated modal analyses in Table 1.

TABLE 1

Eigenfrequencies of elastic mode shapes, experimental and simulation data, mode numbering based on simulation I (element size ⩽ 5 cm), simulation II (element size ⩽ 2·5 cm)

Mode	Eigenfrequencies (Hz)			Description
	Experiment	Simulation I	Simulation II	
1	19·3	19·3	19·3	Lower panel, rear part, first mode
2	20·4	20·2	20·3	Upper panel, front part, first mode
3	23·6	23·7	24·0	Rear panel, global, first mode
4	23·3	27·8	27·9	Lower panel, rear part, second mode
5	28·1	28·1	28·0	External beam frame, first mode
6	29·2	28·6	28·8	Lower panel front, upper panel rear
7	30·5	29·8	30·0	Almost same as mode 6
8	—	35·5	35·7	Upper panel, front part, second mode
9	37·1	36·9	37·2	Side panels and others
10	39·3	38·2	38·7	Front panel, upper part, first mode
22	55·7	54·2	54·6	External beam frame, second mode
24	57·1	56·6	57·3	Front panel, upper part, second mode

welding joints and correct modelling of the free length of the beam frame. Although the beam structure on the front panel is significantly stiffer than the panel itself, an important interaction can be observed. This interaction is expressed by modes 10 and 24. These modes show vibrations of the upper part of the front panel and vibrations of the external frame. The frequencies match very well.

It is important to mention in connection with mode 24 that the idealized shape being provided by finite element analysis is not found in the experiment. This mode can be identified clearly, though. However, the displacements in the left part of the panel (looking from rear to front) are about twice that of those in the right part.

A few more modes can be identified in the experiment and simulation. One example is the rear panel where both of the second mode shapes are clearly observed. Since these modes hardly effect the acoustic noise transfer function as being described later, we dispense with their detailed description.

Only a few remarks are given for the fluid modes inside the box. Assuming hard reflecting walls, the lowest fluid mode can be expected at 113 Hz. Successively, higher modes can be found. It is mentioned at this point that with hard reflecting walls provided, an additional rigid body mode at 0 Hz occurs. However, this mode can exist only if a slowly increasing pressure inside the model does not escape. Gaps between welding spots, joints and bore holes definitely destroy this assumption. We are going to discuss this matter later with the noise transfer function.

Finally, in this section we would like to briefly discuss issues of the numerical reliability of the structural model with respect to its discretization. As mentioned in the previous section, two finite element models of the structure are considered: one model consists of elements up to 5 cm length, and the other one up to 2·5 cm length. Comparison of the eigenfrequencies of these two meshes should suffice for such a check. In general, one observes about 1% deviation between eigenfrequencies of matching modes up to a frequency of 150 Hz. Table 2 presents the number of eigenfrequencies up to certain frequency bounds. These numbers coincide well in the range up to 150 Hz. Moreover, these counts provide an impression of the modal density of the complex model.

TABLE 2

Number of eigenfrequencies of elastic mode shapes (rigid-body modes excluded) below certain frequency limits for simulation I (element size $\leqslant$ *5 cm), simulation II (element size* $\leqslant$ *2·5 cm) and the optimized structure (discretization as in simulation I)*

	Number of eigenfrequencies					
Type	50 Hz	100 Hz	150 Hz	200 Hz	250 Hz	300 Hz
Simulation I	20	61	108	159	217	275
Simulation II	19	61	108	156	212	268
Optimized	19	58	104	153	211	266

4. STRUCTURAL AND NOISE TRANSFER FUNCTIONS

4.1. STRUCTURAL TRANSFER FUNCTION

Structural transfer functions are available from the modal analysis. Furthermore, they are measured at 22 locations using accelerometers when the structure is excited by a sweep sine force signal at the left corner of the external beam frame in front of the box. A shaker of type LDS V450 is used. The harmonic accelerations are then integrated twice to find the structural transfer functions, i.e., the displacements due to a unit force excitation. Measured transfer function values are available in steps of 0·25 Hz.

A corresponding configuration is applied to the simulation model. A finite element approach is used. Further, we assume a harmonic time dependence of the force excitation as $\hat{f}(\vec{\mathbf{x}}, t) = f(\vec{\mathbf{x}})\,\mathrm{e}^{\mathrm{i}\omega t}$. Vector $\vec{\mathbf{x}}$ represents the position in space, ω is the circular frequency and t and i denote time and imaginary unit respectively. The structural transfer function is now calculated by solving the linear harmonic system of equations

$$\mathbf{A}(\omega)\mathbf{u}(\omega) = \mathbf{f}(\omega) \tag{1}$$

for the harmonic displacements assembled in the column matrix **u**. The other column matrix **f** contains the nodal excitation force vectors. **A** is the global system matrix of finite elements more commonly known as the dynamic stiffness matrix given by

$$\mathbf{A}(\omega) = \mathbf{K} + \mathrm{i}\omega\mathbf{B} - \omega^2\mathbf{M}. \tag{2}$$

It consists of the (static) stiffness matrix **K**, the damping matrix **B** and the mass matrix **M**. Apparently, the harmonic displacement of a single node appears as a vector. However, in the current example we have clearly defined major displacement directions that coincide with the directions of the Cartesian co-ordinate axes. These are the vertical direction for the excitation point and a point at the lower panel, the horizontal one for the front and the rear panel. Figure 6 gives an impression of the structural transfer functions for points at these four parts of the construction.

The best coincidence between the experiment and simulation is observed for the excitation position. For the point at the front panel, both functions show a very similar behaviour in the range between 20 and 60 Hz. However, matching gets worse the longer the transfer path becomes. Examples for the lower and rear panels are shown in Figure 6.

While for short transfer paths a comparison between the experiment and simulation appears to be simple or at least possible, this comparison is difficult or even impossible for longer transfer paths. A useful strategy that is often applied for complex structures is a suitable averaging. This average displacement $\bar{u}$ is evaluated in a certain frequency

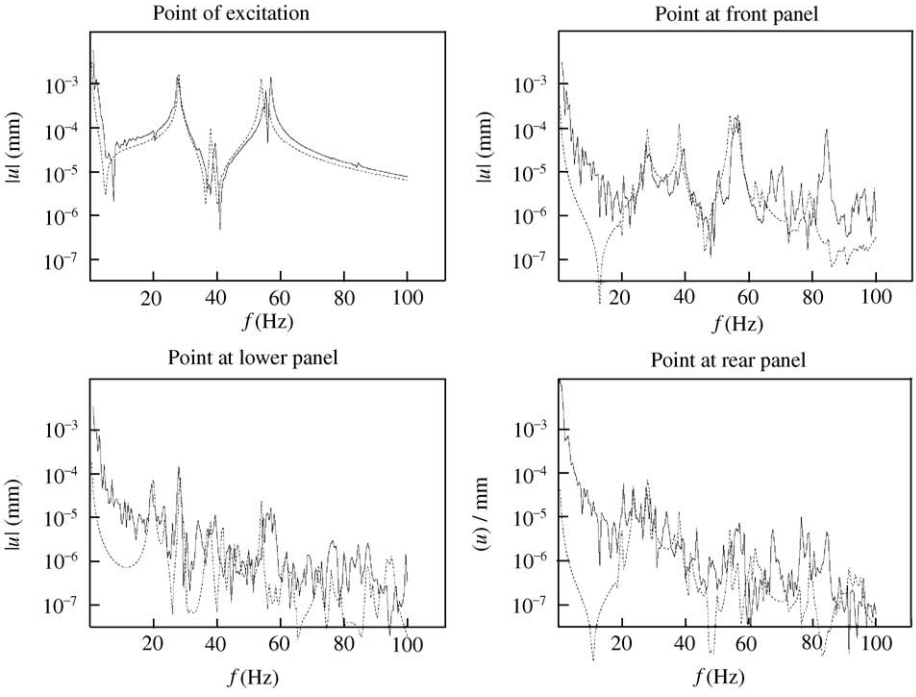

Figure 6. Structural transfer functions measured and calculated for four different points, excitation at the external base-frame, averaging *not* included: ——, experiment; ·····, simulation.

window of size $2\Delta\omega$ (reaching from $(\omega - \Delta\omega)$ to $(\omega + \Delta\omega)$ using the formula

$$\bar{u}(\omega) = \frac{1}{2\Delta\omega} \int_{\omega-\Delta\omega}^{\omega+\Delta\omega} u(\omega)\,\mathrm{d}\omega. \tag{3}$$

Herein, in all applications, a 10 Hz window ($\Delta\omega = 5$ Hz) is used. The average intervals are suitably adjusted at the lower and upper bounds of the complete frequency range. The resulting transfer functions that have been discussed above are plotted again in Figure 7.

Although the general information of Figure 6 is the same in Figure 7, the latter is much easier to survey. Especially for model adjustments, an average is advantageous and highly recommended.

In the process of modelling, some additional measures and tests are included to achieve a better adjustment of experimental and calculated transfer functions. The structural transfer function proves, more than the mode shapes, to be highly sensitive in terms of the coupling conditions between both frames, in particular, the location and the number of coupling points.

As in many other applications of modelling, the structural damping accounts for another major challenge. Owing to practical reasons, especially simplicity of the simulation model, it was decided to use mode-specific damping ratios. Hence, each mode is supplied with its own damping ratio. However, the experimental modal analysis indicates very low modal damping ratio. For the lower vibration modes being identified, ratios 0·1–0·2% are found. The experimentally discovered modes between 50 and 60 Hz, cf. Figure 5, provide values of approximately 0·7%. In general, modal damping ratio estimates are less than 1% rather tending to zero than to greater values.

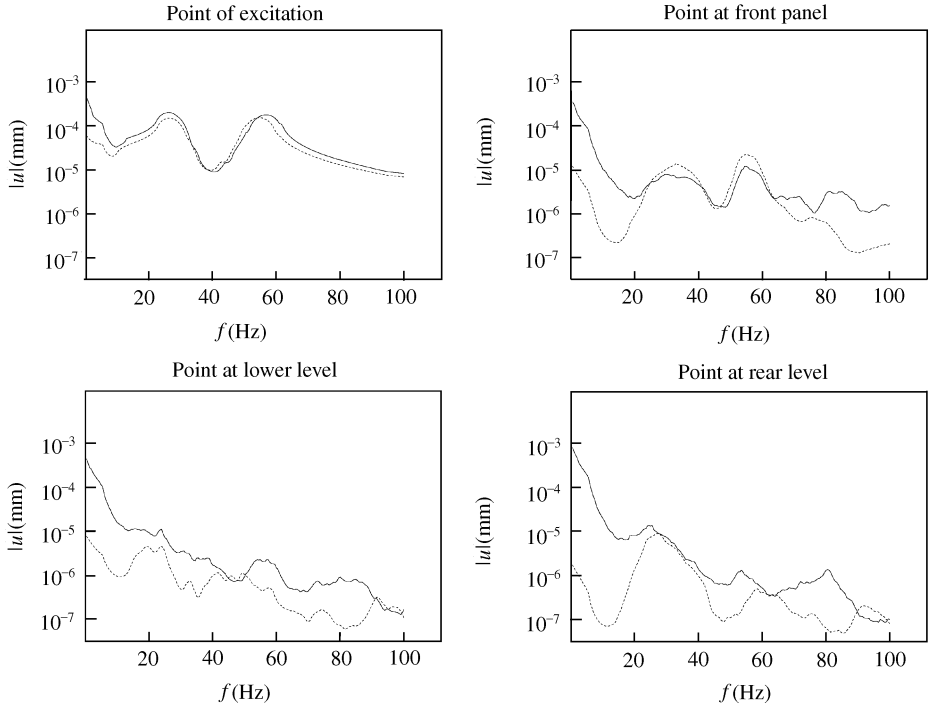

Figure 7. Structural transfer functions measured and calculated for four different points, excitation at the external base-frame, 10 Hz-averaging included: ——, experiment; ……, simulation.

Note that the structural transfer functions of the simulation underestimate the measured ones. Most likely, this is a result of the high sensitivities of the welding joints and welding spots. More realistic values for the coupling elasticity are unknown but highly desirable. Vlahopoulos *et al.* [25] determined transfer coefficients for spot welds using energy finite element formulations. However, their approach holds for higher frequencies. For lower frequencies, their test data show an energy dissipation, but this cannot be simply transferred to the very low-frequency range and somewhat different configuration at the edges.

4.2. NOISE TRANSFER FUNCTION

In what follows, the sound pressure level at certain position inside the box due to an unit force excitation at the external frame is called the noise transfer function.

Noise transfer functions are measured at three locations inside the box. Their positions are marked by M_1, M_2 and M_3 in Figure 1. The first two positions are arbitrarily chosen, the third is located in the centre of the box. As mentioned previously, the microphones are hung through bored openings in the upper panel. Similar to the structural transfer functions in the previous subsection, the structure is excited by a sweep sine signal given by a shaker of type LDS V450. The sound pressure is measured using precision sound level meter of type PSI 00024.

The calculation procedure of the noise-transfer function is identical with the one proposed in reference [28]. To resume briefly, one starts with the structural transfer function, i.e., harmonic displacements of the nodes of the finite element mesh assembled in

the column matrix **u**. For consideration of noise emission inside the box, the number of nodes are split into noise-emitting and non-noise-emitting ones. It is assumed that the flat panels emit noise into the box and the frames do not. This is a simplification that may be justified by the size of the frame compared with the fluid wavelength. Near the edges of the box, elements of the flat panel and elements of the frame coincide. Their contribution should be considered only once.

For the set of noise-emitting nodes, the displacements are multiplied by $i\omega$ to calculate the harmonic velocity. Scalar multiplication of each nodal velocity vector with its normal vector (directing outwardly) provides the normal components of the particle velocity of the structure. Assembling the components of all normal vectors in a matrix **N** and extending equation (1) allows one to formulate

$$\mathbf{v}_s(\omega) = i\omega \mathbf{N}\,\mathbf{A}^{-1}(\omega)\,\mathbf{f}(\omega), \tag{4}$$

where $\mathbf{v}_s$ denotes the (normal) particle velocity of the structure. The sound pressure at certain positions inside the structure can be calculated simply by a scalar multiplication of a column matrix of influence coefficients **b** and that of the nodal particle velocities $\mathbf{v}_s$. One can write for the sound pressure p_i

$$p_i(\omega) = \mathbf{b}^{\mathrm{T}}(\omega)\,\mathbf{v}_s(\omega) = i\omega \mathbf{b}^{\mathrm{T}}(\omega)\,\mathbf{N}\,\mathbf{A}^{-1}(\omega)\,\mathbf{f}(\omega). \tag{5}$$

These influence coefficients allow an explicit mapping of the particle velocity of the structure to the sound pressure, i.e., they represent the solution of the fluid's boundary value problem. Hence, they depend on the geometry of the fluid domain, the frequency, the boundary admittance or impedance, respectively, and, obviously, on the position of the internal point. However, if the geometry does not change significantly, if the admittance remains constant and if the sound pressure is required at few positions only, acoustic influence coefficients account for an efficient tool for structural acoustic optimization since they have to be calculated only once in the entire optimization process. Examples of their application can be found in references [21–23]. The influence coefficients is calculated using the non–commercial boundary element–based code AKUSTA. A reference that confirms reliability of this code can be provided [27].

Another problem that arises in the context of modelling fluid domains for acoustic calculation is the choice of suitable boundary conditions. Often, this question is evaded and hard, i.e., fully reflecting walls are assumed. This is equivalent to a vanishing boundary admittance value. Further, one can expect standing wave phenomena if viscous damping can be neglected. In that case, however, one should also expect infinite sound pressure values at eigenfrequencies. Since there is an eigenfrequency at 0 Hz for closed domains and hard reflecting walls, this assumption requires that when uniformly and slowly increasing the static pressure inside the domain, the fluid must not escape. While for a well-sealed sedan cabin this requirement is fulfilled, cf. reference [30], it does not seem realistic here.

Since realistic values for the boundary admittance in this case are not available, a comparison between hard reflecting walls and an (arbitrarily chosen) value is presented. For that, we use the boundary admittance of an infinite plate as follows [31]:

$$Y_0(\omega) = \frac{1}{(\rho_f c - i\omega m_s')} = \frac{1}{(\rho_f c - i\omega \rho_p h)}. \tag{6}$$

The fluid density and speed of sound are represented by ρ_f and c, respectively, m_s' denotes the specific mass of the plate being equal to the product of the plate density ρ_p and its thickness h. Clearly, this choice is an arbitrary one and will, therefore, not be applicable in

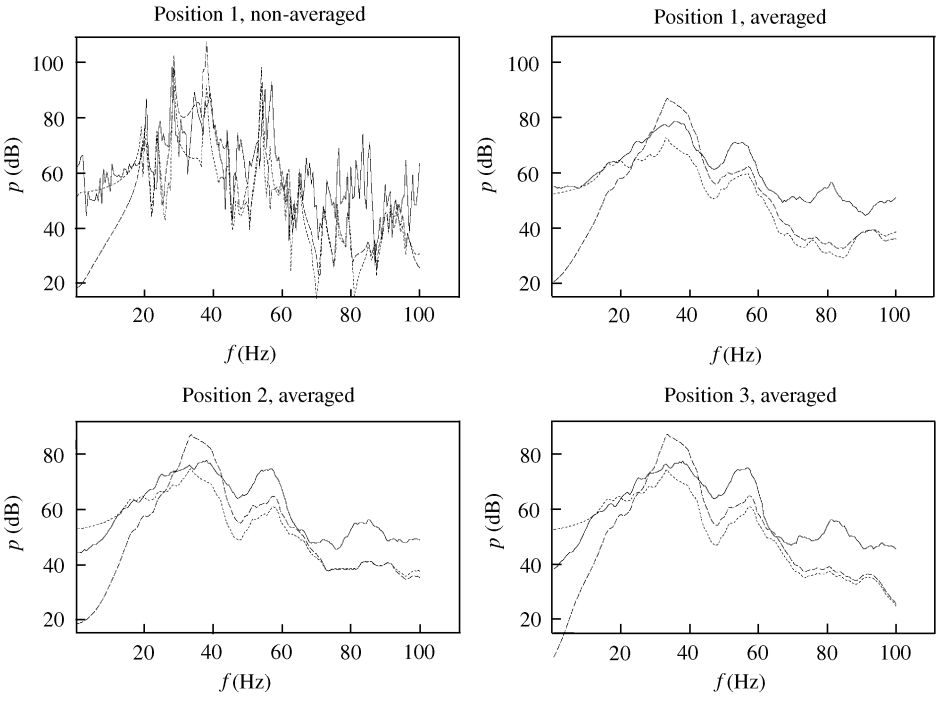

Figure 8. Noise transfer functions at three positions inside the box, experimentally determined functions versus simulation, two boundary admittance values applied as fluid boundary condition: ——, experiment; ……, simulation, $Y = 0$; --------, simulation, $Y = Y_0$.

the low-frequency range that is considered here. Results for this case are presented to show some possible effects and to emphasize the significance of reliable values of the boundary condition.

Figure 8 contains noise transfer functions for the three positions, measured and simulated data. The need for an averaging is confirmed when looking to the upper-left subfigure. It shows the non-averaged noise transfer functions for the first position. Hardly any substantial information can be taken from this picture.

Comparison between the experiment and simulation shows that the transfer functions of simulation and experiment generally behave similarly. For low frequencies ($\leqslant 15$ Hz), the experimentally determined noise transfer function is found between the simulation results. Choice of hard reflecting walls overestimates, a boundary admittance as given above underestimates the noise transfer. This frequency range of the noise transfer function should not be overvalued though. Experimental data below 15 Hz can be expected to contain substantial uncertainties. For the first peak, the situation is the other way around as it is for very low frequencies. Use of rigid walls underestimates, use of the non–zero admittance overestimates the measured data. However, one can realize for frequencies above 10 Hz that hard reflecting walls generally lead to noise transfer functions that either look similar to the experimental one or underestimate these data as the simulated structural transfer function did before.

The calculated functions for non–zero boundary admittances show a considerable deviation from the zero condition. This deviation becomes small above 60 Hz. In Figure 7, we observe an overestimation of the vibration amplitudes of the front panel, an underestimation for the lower panel and good matching for the rear panel in the frequency

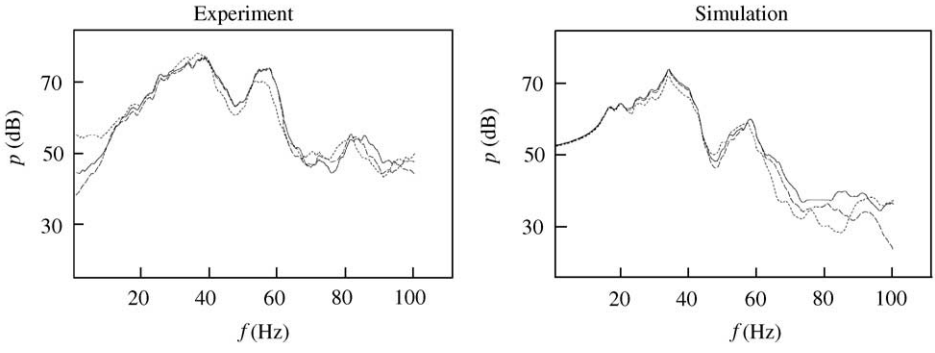

Figure 9. Noise transfer functions at three positions inside the box, comparison of three measured functions (left) and three computed for hard reflecting walls (right): ....., position 1; ——, position 2; --------, position 3.

range between 25 and 40 Hz. Both side panels agree as well. A panel contribution analysis will be provided in the optimization section but it should be remarked here that for a chosen frequency of 38 Hz the front panel, both side panels and the rear one contribute most to the sound pressure at the internal point 2. Hence, an underestimated noise transfer function does not seem very realistic. Suitable values for the boundary condition are desirable.

Moreover, Figure 9 indicates that hard reflecting walls as boundary condition for the fluid may be insufficient for acoustic simulation. This is indicated when comparing the measured noise transfer functions for three positions. We observe that the peak between 50 and 60 Hz is several decibels lower at position 1 compared with the other two positions. Such a behaviour cannot be explained for hard reflecting walls in a frequency range of about half of the first acoustic eigenfrequency (except the rigid-body mode at 0 Hz). A comparison between the corresponding simulation data shows that only much smaller differences are expected between these functions. Note that position 1 is the closest position from the front panel that is likely responsible for this peak, cf. Figure 5, modes 22 and 24.

It can be observed that the peak between 50 and 60 Hz is much smaller in the simulation, cf. Figure 7. It is assumed that this is due to the non–perfect second mode of the front panel that has been discussed in the previous section. The simulation uses a more idealized mode of two loops. These loops look like a dipole, cf. Figure 5 (lower left subfigure), and cancel each other. This assumption fails in reality since both loops have significantly different amplitudes. Several trials to model this behaviour failed because either unrealistic geometry would have been required or the eigenfrequency was shifted away from the desired range. In the end, it is found satisfying that the simulation can supply this peak but not as high as the experiment.

Finally, we can resume that, in general, a good agreement between the experiment and simulation is achieved up to a frequency of 60 Hz. The upper frequency limit corresponds to the upper limit from structural transfer functions especially for the front panel. The simulation model is too stiff for higher frequencies. This is likely due to idealized coupling conditions between the beam frames and the panels.

5. VERIFICATION OF THE SIMULATION MODEL

After building the calculation model it must be verified to experience its reliability. For this purpose, a mass is added to the metal sheet. This mass consists of a compact steel block

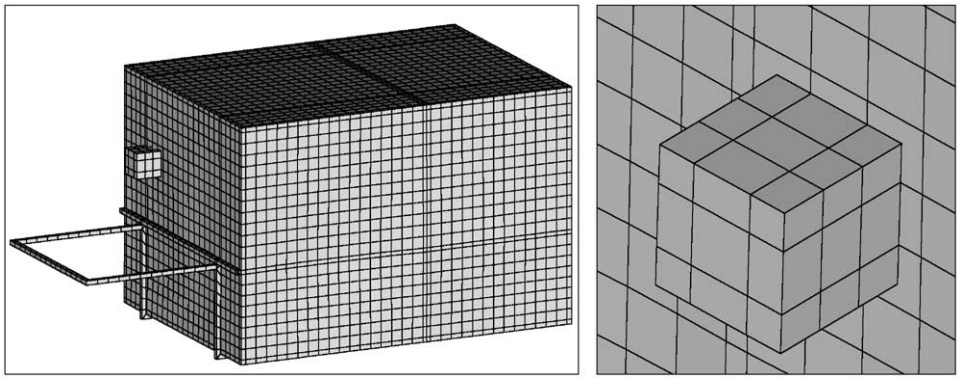

Figure 10. Added mass structure, global view (left), close-up view (right).

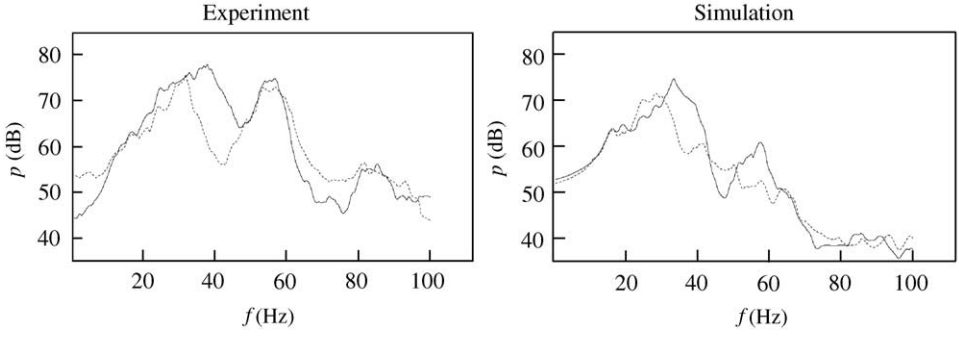

Figure 11. Noise transfer functions at position 2 for added mass: ——, original; ....., added mass.

that is mounted to the panel by just one screw. It weighs 10 kg. The front panel is chosen since this part of the box seems to contribute most to the noise inside. A heavy additional structure should significantly change the modal properties of the front panel.

Solid three–dimensional brick elements are used to model this block. Coupling of this new structure to the front panel is realized by coupling four single nodes. Hence, there is a more distributed coupling in the calculation model. Mainly, this is subject to numerical considerations. A concentrated coupling at just one node of the front panel may cause unexpected singularities. With respect to the physical model, one can even argue that the screw and washers on both sides of the panel rather represent a distributed coupling than a concentrated one. The position of the added structure is shown in Figure 10.

Position and size of the added mass allow one to predict that modes 10 (Experiment: 39·3 Hz) and 24 (Experiment: 57·1 Hz) especially are changed. This actually happens. Modification of mode 10 reduces the noise transfer function, see for example for position 2 in Figure 11. However, modification of mode 24 in the experiment reduces vibration of the right loop while the left remains. Mode 24 vanishes in the simulation after modification. This is likely due to idealization of modelling as discussed in the previous sections.

Generally, one can conclude that the simulation model represents the modification in the noise transfer function. This claim holds for frequencies up to 50 Hz. Furthermore, the reason for different behaviour of simulation and experiment for the range between 50 and 60 Hz can be explained. Hence, the range of reliability of the simulation model reaches up to

60 Hz if we are careful with the peculiarities of the front panel. Apparently, this essentially verifies certain reliability for the front panel only. However, it was shown in the previous section that this panel contributes most to the noise inside.

6. OPTIMIZATION OF THE STRUCTURE

6.1. FEASIBLE MODIFICATIONS

It is one idea of this project to provide evidence that a design optimization of a complex structure can actually lead to an improved physical construction. As explained in the first section, this evidence presupposes a non–destructive modification of the model. For that reason, a decision is made that two panels are to be selected for modification. Initially, two beams per panel should be attached. However, this technique proved to be unsuited from the production–engineering point of view since both panels are too uneven. Thus, the beams are to be mounted while washers are used to bridge the local distances between straight beams and distorted metal sheets. This technique should ensure that the beams are coupled tightly but do not modify the uneven geometry of the metal plate. It is emphasized that welding of the beams would likely change the geometry of the panel. Moreover, the chance of dismantling would have been spoiled.

The optimization concentrates on the noise transfer function of position 2. This position is chosen because the corresponding noise transfer functions of the simulation and experiment matched better than for position 1. The other one is not selected because of its special position in the centre of the box.

A panel contribution analysis is made to select two surfaces for modification in the optimization process. The approach is similar to the one originally proposed by Ishiyama *et al.* [32] and improved by Adey *et al.* [33]. Following their approach or returning to equation (5), one can calculate the sound pressure p_i at a specified position inside the box as

$$p_i = \sum_{j=1}^{N_p} \sum_{k=1}^{N_j} b_{jk} v_{s_{jk}}. \tag{7}$$

Here, N_p and N_j denote the number of panels and the number of nodes per panel respectively. As explained above, b_{jk} and v_{sjk} represent nodal values of the influence coefficients and the particle velocity of the structure respectively. Summing up all nodal contributions of one panel supplies the panel contribution p_c

$$p_{c_j} = \sum_{k=1}^{N_j} b_k v_{sk}. \tag{8}$$

The value p_{c_j} describes the sound pressure at the internal point if only the jth panel contributes to the noise inside.

Apparently, panel contributions depend on the frequency and position. However, Figure 9 proves that for frequencies below 60 Hz, hardly any dependence on the location of the internal point can be observed. For a frequency of 60 Hz, the wavelength is about 5·7 m. Usually, the decrease of high peaks in the noise transfer function is a primary target for construction. For that reason, frequencies 38 and 56 Hz are chosen for the panel contribution analysis. These frequencies correspond to maxima in the noise transfer function of position 2.

Table 3 contains the contributions of all panels for the above-chosen frequencies. Unquestionably, we identify the front panel and the lower panel as those that contribute most to the interior noise. However, remarkable low contribution of the front panel to the noise at 56 Hz raises the question of the second front panel mode again. As discussed

TABLE 3

Panel contributions to sound pressure at position 2 at two frequencies

	Contribution of panel in decibels						
Frequency	Front	Lower	Upper	Right	Left	Rear	All panels
38 Hz	91·4	43·5	54·8	74·4	71·8	62·9	93·7
56 Hz	46·8	65·9	43·8	50·1	44·9	38·6	69·3

previously, both vibration loops cancel each other. Hence, the part of the surface that shows the greatest displacements emits noise to the inside negligibly.

6.2. DESIGN PARAMETERS AND OBJECTIVE FUNCTION

In the context of feasible modifications, it has been mentioned that two beams can be added to both, the front and lower panels. Obviously, these beams must not cross each other. For numerical reasons that will be discussed later in this subsection, we require that they all are parallel. Hence, two parameters per added beam have to be controlled: one for the position and the other for the length. For simplicity, we require that every beam is mounted symmetrically (presupposing an approximately symmetric construction). Consequently, for two beams per panel and two design parameters per beam, the model can be modified by eight parameters.

A numerical problem that occurs when fixing these beams to the surface panels consists in coupling both structures. As can be seen in Figure 2 the area model is prepared to connect virtually coincident nodes. Hence the distances between two nodes are very short and it is clarified as to which node is to be coupled with another. The situation for a continuously shifted beam is more complicated. If the beam coincides with a line of nodes of the panel elements, automated mapping for coupling is simple. However, when this beam is just located between two lines of nodes, this mapping is not as clear. Furthermore, the jump of the coupling from one line of nodes to another causes certain discrete properties. Hence it was decided that beam positioning is allowed only along a line of nodes and the parameter domain between is interpolated.

The objective function has been discussed in reference [28]. Recalling this function, one can write

$$F = \frac{1}{(\omega_{max} - \omega_{min})} \int_{\omega_{min}}^{\omega_{max}} \Phi\{p_L(\omega)\}\, \mathrm{d}\omega. \tag{9}$$

The operator $\Phi\{\ \}$ applied to the sound pressure level p_L represents a kind of a weighting function. An example for this weighting function is

$$\Phi\{p_L\} = \begin{cases} (p_L - p_{Ref})^n & \text{for} \quad p_L > p_{Ref}, \\ 0 & \text{for} \quad p_L \leqslant p_{Ref}. \end{cases} \tag{10}$$

The exponent n controls the type of average. For $n = 1$, equation (9) leads to the mean value, where only values higher than a certain reference level p_{Ref} are taken into account. Similarly, for $n = 2$, this form provides the mean squared value. The major advantage of the $n = 2$ form is that high-level peaks are higher valued than low-level parts of the function. This helps to reduce these high-level peaks during an optimization procedure and avoids

deep valleys as compensation of high peaks. This effect is increased by using a reference level higher than the lowest values in the noise transfer function.

Herein, the optimization process is directed to minimize the objective function, equations (9) and (10), using the exponent $n = 2$ and the reference sound pressure level $p_{Ref} = 55$ dB.

The finite element code ANSYS that is applied for structural analysis is used for optimization. Due to the above-sketched numerical problem, a gradient-based method fails. A gradient-based method could work well in this case if the partially discrete character of this problem is considered. A random iteration is very competitive for this problem. It is simple to adjust this method to the stepped design modifications. Additional trials using a scan algorithm can be reported. However, best results are found by random iteration.

6.3. OPTIMIZED DESIGN AND ITS MODE SHAPES

One reason for successful application of a random iteration method is the unique and easy-to-understand solution for most of the optimization variables. So, in all cases the optimal length of the beams is equal to their maximum length. Moreover, the beam in the upper part of the front panel is to be placed to calm down the first and second vibration modes of this panel, in total being modes 10 and 24. Hence, only three variables remain to be optimally controlled.

A total of about 500 computations of the objective function—single evaluation of the objective function takes about 30 min CPU time on an SGI/Origin 2000—provided the optimized design, see Figure 12. The photograph in Figure 1 shows the stiffeners on the front panel. The locations of the stiffeners on the front panel look quite reasonable and,

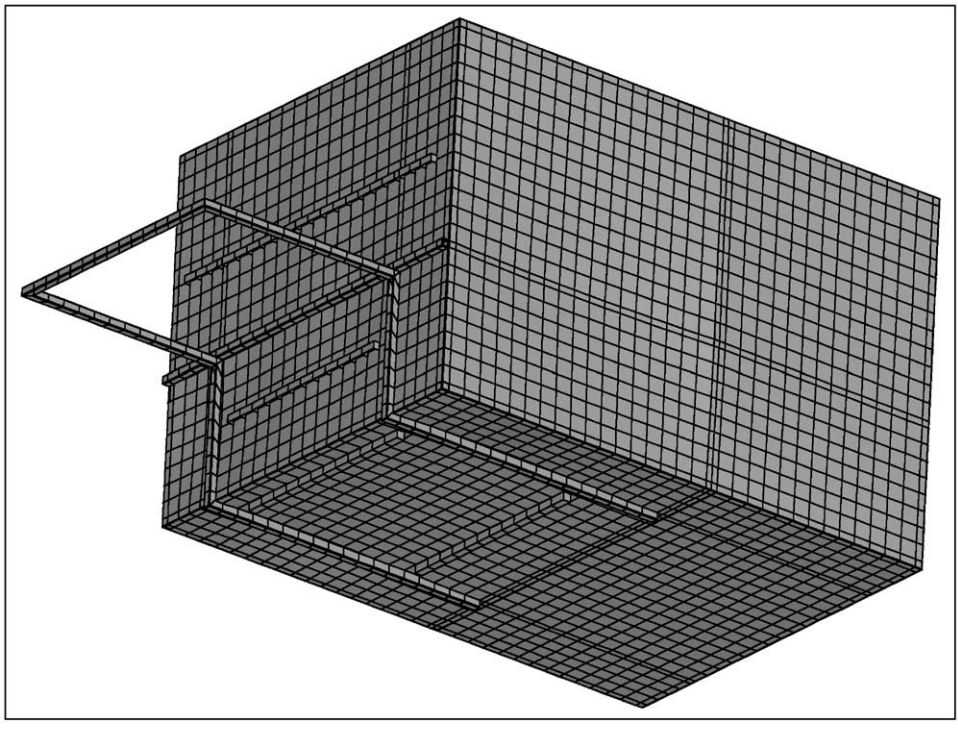

Figure 12. Optimized model: four additional beams on front and lower panels.

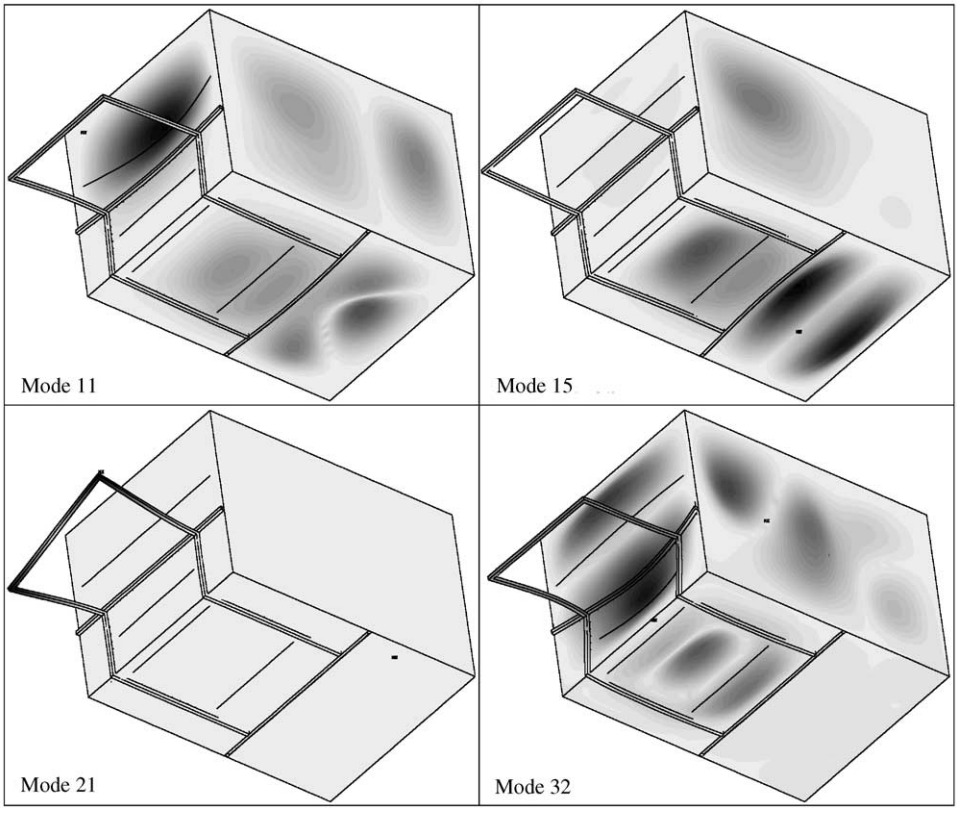

Figure 13. Selected mode shapes of optimized model: Mode 11: 42·0 Hz, Mode 15: 45·9 Hz, Mode 21: 53·8 Hz, Mode 32: 64·8 Hz.

most likely, an engineer would design this part in a similar way. The solution for the lower panel appears somewhat more surprising. While one of the stiffeners is found in the centre of the lower panel, the other one is shifted to the front edge. Due to the internal frame construction, this part of the plate is very stiff in the direction of the added beam. Therefore, we assume that further stiffening of the lower panel would possibly increase the interior noise. The results of modal analysis show that the vibrations of the lower panel do not account for a complete mode shape. Starting with modes 6 and 7 of the original structure, there is at least one more panel vibrating together with the lower one at the same natural frequency.

Staying with these two modes (6,7) of the original simulation model, see Figure 4, we realize that these two modes reduce to one in the optimized design. This remaining mode consists of vibrations of the upper panel only. It is assumed that the positioning of the stiffener was mainly focused on destruction of this mode shape.

Mode 10 of the original model, see Figure 5, increases by about 10% up to 42 Hz as the 11th mode in the optimized one, see Figure 13. It can be seen that, compared with the original, the contribution of other than the front panel increases. A typical vibration mode shape of the lower panel is found at 45·9 Hz. Mode 22 of the original becomes mode 21 in the optimized model. In the original model, this mode is slightly coupled with the second mode of the upper front panel, see Figure 5. In the optimized model, the external frame is the only vibrating part at this frequency, see Figure 13. While mode 24 of the original does

not occur in the optimized design, we would like to show one more mode of high mobility of the front panel. It is mode 32 at 64·8 Hz. One can clearly recognize that the stiffener in the upper part of the front panel helps to separate vibration loops of the shell and, apparently, it controls the corresponding eigenfrequency.

It is widely assumed that stiffening of a structure reduces the noise that is emitted. It appears much more difficult to measure the stiffness, in particular, for complex structures. Defined as force per displacement, stiffness cannot be considered as a local measure. More globally oriented measures for stiffness are the lowest eigenfrequency or the number of modes up to a certain frequency limit. It was shown in reference [23] that static stiffness does not necessarily ensure better acoustics. Moreover, it was shown there that even the decrease of the first natural frequency by about 35% can remarkably decrease the modal density and improve the acoustic behaviour of the structure. It was proposed in that paper to measure the stiffness for acoustic purposes in the number of modes up to a certain frequency.

The modal densities of the original and the optimum are given in Table 2. We realize that the number of modes up to certain frequency limits decreases very little for the optimized design. The new shape mainly takes advantage of a selective stiffening that destroys certain modes being unfavourable for acoustics.

6.4. NOISE TRANSFER AND OBJECTIVE FUNCTIONS OF OPTIMIZED DESIGN

A comparison between the experiment and simulation of the original and the optimized models at positions 1–3 are shown in Figure 14. Clearly, the first wide peak from 20 to 40 Hz is significantly decreased. The second peak between 55 and 60 Hz is still observed in the experiment. Simulation provides a similar peak at somewhat lower frequencies but this one likely corresponds to another mode shape than the one observed in the experiment. It is in good agreement with the model verification using the added mass that the second peak at about 55 Hz does not vanish although predicted. Note that in the frequency range up to 60 Hz hardly any differences between the data at different positions can be observed.

Table 4 contains the values of the objective function for different parameters, cf. equations (9) and (10), for simulation and experiment. While the optimization process has been

TABLE 4

Difference of objective function between original and optimized model, results for different parameters of the objective function, equations (9) *and* (10)*, comparison of simulation and experiment* (*optimization process provided minimum for* $n = 2$ *and* $p_{Ref} = 55\,dB$ *in the frequency range between* 0 *and* 100 *Hz*)

		Decrease of objective function in decibels					
		0–100 Hz		0–60 Hz		10–50 Hz	
n	p_{Ref} (dB)	Simulation	Experiment	Simulation	Experiment	Simulation	Experiment
1	0	3·4	1·3	4·5	3·3	4·9	6·3
1	55	2·4	2·2	4·0	4·3	5·4	6·3
2	0	3·6	1·8	4·8	3·8	5·2	6·4
2	55	4·1	3·3	5·2	4·7	6·3	6·7

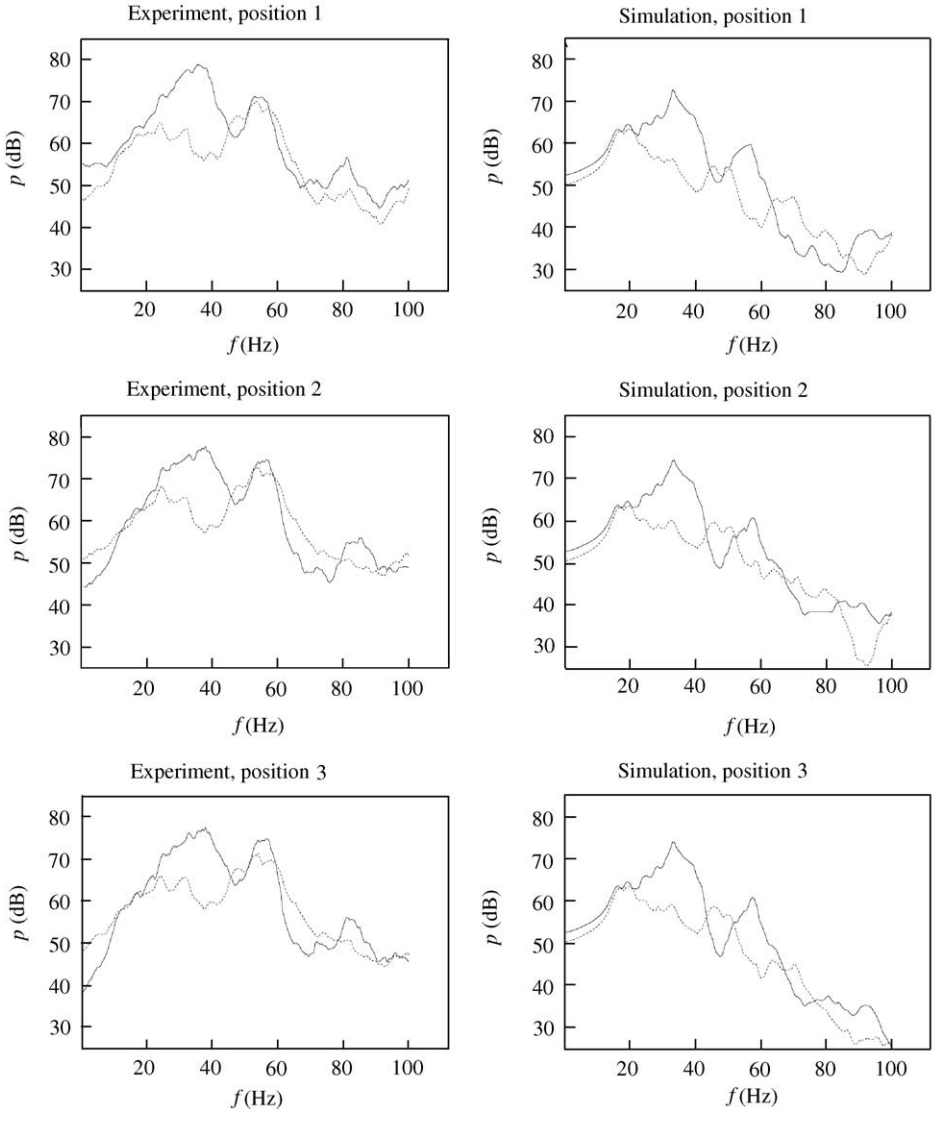

Figure 14. Noise transfer functions at three positions, determined for original and optimized models by simulation and experiment: ——, original; ....., optimum.

controlled by the parameters $n = 2$ and $p_{Ref} = 55$ dB in the frequency range between 0 and 100 Hz, these data are compared with the objective function values for $n = 1$ and/or $p_{Ref} = 0$ dB. In the optimization process, the objective function is decreased by 4·1 dB while the experiment still shows 3·3 dB improvement.

However, in the case of simulation the noise transfer function does not exceed the reference level of $p_{Ref} = 55$ dB for frequencies above 60 Hz. For that reason, the data for a reduced frequency range are also shown. Now, the simulation predicts 5·2 dB improvement, whereas the experimental test validates 4·7 dB.

With respect to the experiment, the reliable frequency range starts between 10 and 20 dB while the reliable frequency range for the structural model ends at about 50 Hz. Thus, the

objective function in this frequency domain is computed as well. Since major peaks and improvements occur in this part of the noise transfer function, the greatest decrease can be reported. Simulation predicts 6·3 dB and the experiment even supplies a 6·7 dB lower objective function.

Generally, trends that have been predicted by simulation can be proved in the experiment. But this statement reduces to the reliable frequency range. More than 6 dB decrease of the objective function can be reported for this range of reliability.

7. FINAL REMARKS

Finally, one can summarize that the entire process from model creation and adjustment, model verification and optimization has been presented in this paper. It is shown that the relatively large decreases of noise transfer that are predicted by simulation and optimization, are also found in the experiment. This verification, however, is impossible if the simulation model cannot predict the major effects that are responsible for noise. In the current application, these effects are well included for frequencies up to 50 Hz. For frequencies above 50 Hz, the simulation model is likely to be too stiff, which is assumed to be due to an insufficiently detailed modelling at the edges and welding joints.

In general, a more reliable model requires more careful modelling techniques for these parts of the structure. Further, a detailed scan of the surfaces seems necessary. This scan should provide the geometry of the panels. Their exact incorporation accounts for another crucial point in the modelling process. It shall be mentioned that yet no word has been said about the phase angles. Phase angles have been considered in the calculation model. But their values were not considered in the modelling process. Obviously, more detailed modelling should include the adjustment of phase angles as well. Apparently, these extensions would significantly increase requirements of manual work. However, doing such a work in a finite period of time remains as one of the key questions in engineering.

The optimization process included positioning and length of additional beams. A case study of the addition of beams to the shell structure of a vehicle roof [33] proved that only little improvements are gained compared with modification of the shell curvature. However, experimental verification of such a case appears difficult and very costly. In general, one should rely on the simulation model once this model is verified.

ACKNOWLEDGMENT

We kindly acknowledge the financial support by the FORD–Werke AG Köln (Germany) where the physical model of the box was constructed. It is further acknowledged, that part of the computations were performed on a SGI Origin2000 supercomputer at the Zentrum für Hochleistungsrechnen of the Technische Universität Dresden.

REFERENCES

1. S. A. HAMBRIC 1995 *Journal of Vibration and Acoustics* **117**, 136–144. Approximation techniques for broad–band acoustic radiated noise design optimization problems.
2. S. A. HAMBRIC 1996 *Journal of Vibration and Acoustics*, **118**, 529–532. Sensitivity calculations for broad–band acoustic radiated noise design optimization problems.
3. J. S. LAMANCUSA *Computers and Structures* **48**, 661–675. Numerical optimization techniques for structural–acoustic design of rectangular panels.

4. J. S. LAMANCUSA and H. A. ESCHENAUER 1994 *American Institute of Aeronautics and Astronautics Journal* **32**, 472–479. Design optimization methods for rectangular panels with minimal sound radiation.
5. J. S. LAMANCUSA 1998 *Journal of Sound and Vibration* **127**, 303–318. Geometric optimization of internal combustion engine induction systems for minimum noise transmission.
6. F. HIBINGER 1998 *Dissertation*, Technische Universität Darmstadt. Numerische Strukturoptimierung in der Maschinenakustik.
7. W. KOZUKUE, C. PAL and I. HAGIWARA 1992 *Computers in Engineering* (*American Society of Mechanical Engineers*) **2**, 15–22. Optimization of noise level reduction by truncated model coupled structural–acoustic sensitivity analysis.
8. C. PAL and I. HAGIWARA 1993 *Finite Elements in Analysis and Design*, **14**, 225–234. Dynamic analysis of a coupled structural–acoustic problem. Simultaneous multi–modal reduction of vehicle interior noise level by combined optimization.
9. C. PAL and I. HAGIWARA 1994 *JSME International Journal*, *Series C*, **37**, 246–251. Optimization of noise level reduction by truncated modal coupled structural-acoustic sensitivity analysis.
10. M. TINNSTEN, B. ESPING and M. JONSSON 1999 *Structural Optimization* **18**, 36–47. Optimization of acoustic response.
11. M. TINNSTEN 2000 *Structural Optimization* **19**, 122–129, 2000. Optimization of acoustic response—a numerical and experimental comparison.
12. S. P. CRANE, K. A. CUNEFARE, S. P. ENGELSTAD and E. A. POWELL 1997 *Journal of Aircraft*, **34**, 236–243, 1997 Comparison of design optimization formulations for minimization of noise transmission in a cylinder.
13. K. A. CUNEFARE, S. P. CRANE, S. P. ENGELSTAD and E. A. POWELL 1999 *Journal of Aircraft*, **36**, 563–570. Design minimization of noise in stiffened cylinders due to tonal external excitation.
14. S. P. ENGELSTAD, K. A. CUNEFARE, E. A. POWELL and V. BIESEL 2000 *Journal of Aircraft* **37**, 165–171. Stiffener shape design to minimize interior noise.
15. A. D. BELEGUNDU, R. R. SALAGAME and G. H. KOOPMANN 1994 *Structural Optimization*, **8**, 113–119. A general optimization strategy for sound power minimization.
16. E. W. CONSTANS, A. D. BELEGUNDU and G. H. KOOPMANN 1998 *American Institute of Aeronautics and Astronautics Journal* **36**, 134–139. Design approach for minimizing sound power from vibrating shell structures.
17. K. NAGHSHINEH, G. H. KOOPMANN and A. D. BELEGUNDU 1992 *Journal of the Acoustical Society of America* **92**, 841–855. Material tailoring of structures to achieve a minimum radiation condition.
18. R. L. ST PIERRE JR and G. H. KOOPMANN 1995 *Journal of Mechanical Design* **117**, 243–251. A design method for minimizing the sound power radiated from plates by adding optimally sized, discrete masses.
19. E. W. CONSTANS, G. H. KOOPMANN and A. D. BELEGUNDU 1998 *Journal of Sound and Vibration*, **217**, 335–350. The use of modal tailoring to minimize the radiated sound power of vibrating shells: theory and experiment.
20. S. T. CHRISTENSEN and N. OLHOFF 1998 *Control and Cybernetics* **27**, 177–198. Shape optimization of a loudspeaker diaphragm with respect to sound directivity properties.
21. S. MARBURG and H.-J. HARDTKE 2002 *Structural and Multidisciplinary Optimization* **24**(1). Efficient optimization of a noise transfer function by modification of a shell structure geometry. Part ii: Application to a vehicle dashboard.
22. S. MARBURG, H.-J. HARDTKE, R. SCHMIDT and D. PAWANDENAT 1997 *Engineering Analysis with Boundary Elements* **20**, 305–310. An application of the concept of acoustic influence coefficients for the optimization of a vehicle roof.
23. S. MARBURG, H.-J. HARDTKE, R. SCHMIDT and D. PAWANDENAT 1997 in *Proceedings of the NAFEMS World-Congress*, Stuttgart, 885–896. Design optimization of a vehicle panel with respect to cabin noise problems.
24. Swanson Analysis System Inc., Houston, ANSYS GUI *Help Manual*, *ANSYS Release* 5·4, 1997.
25. N. VLAHOPOULOS, X. ZHAO and T. ALLEN 1999 *Journal of Sound and Vibration*, **220**, 135–154. An approach for evaluating power transfer coefficients for spot-welded joints in an energy finite element formulation.
26. F. IHLENBURG 1998 *Finite Element Analysis of Acoustic Scattering*, Vol. 132, *Applied Mathematical Sciences*. Berlin, Heidelberg, New York: Springer-Verlag.
27. S. MARBURG 2002 *Journal of Computational Acoustics* **10**(1). Six elements per wavelength. Is that enough?.

28. S. MARBURG 2002 *Structural and Multidisciplinary Optimization* **24**(1). Efficient optimization of a noise transfer function by modification of a shell structure geometry. Part i: Theory. Accepted for publication.
29. H. VAN DER AUWERAER, W. LEURS, P. MAS and L. HERMANS 2000 in *Proceedings of IMAC-XVIII*: *A Conference on Structural Dynamics*, *San Antonio*, *TX*, Vol. 2, 763–771. Society for Experimental Mechanics Inc. Modal parameter estimation from inconsistent data sets.
30. S. MARBURG and H.-J. HARDTKE 1999 *Engineering Analysis with Boundary Elements* **23**, 737–744. A study on the acoustic boundary admittance. Determination, results and consequences.
31. L. CREMER and M. HECKL 1996 *Körperschall*: *Physikalische Grundlagen und technische Anwendungen*. Berlin, Heidelberg, New York: Springer-Verlag.
32. S.-I. ISHIYAMA, M. IMAI, S.-I. MARUYAMA, H. IDO, N. SUGIURA and S. SUZUKI 1988 *SAE paper* 880910 195–205. The application of ACOUST/BOOM—a noise level prediction and reduction code.
33. R. A. ADEY, S. M. NIKU, J. BAYNHAM and P. BURNS 1995 in *Computational Acoustics and its Environmental Applications* (C. A. Brebbia, editor), 181–188. Computational Mechanics Publications, Berlin: Springer. Predicting acoustic contributions and sensitivity application to vehicle structures.